A Computational Method for Oleo-Acoustics, Application to Hydraulic Shock Absorbers

B. Koren
CWI
P.O. Box 94079, 1090 GB Amsterdam, The Netherlands

P.F.M. Michielsen and J.W. Kars
KONI B.V.
P.O. Box 1014, 3260 AA Oud-Beijerland, The Netherlands

P. Wesseling
Delft University of Technology
P.O. Box 5031, 2600 GA Delft, The Netherlands

Abstract

To predict high-frequency oil-flow phenomena in hydraulic-shock-absorber designs, a mathematical-physical model is proposed. The model consists of the 2-D unsteady Euler equations in axial-symmetric coordinates and an appropriate equation of state for oil. The main topic of the paper is the development of a numerical method for these equations. A new Osher-type flux-difference splitting scheme is derived for it. The mathematical-physical model and its numerical approximation are applied to a simplified part from a shock-absorber design. The method is promising as far as more realistic computations are concerned.

AMS Subject Classification (1991): 65M20, 65M25, 65M60, 76N10, 76Q05.
Keywords and Phrases: high-frequency oleodynamics, hydraulic-shock-absorber design, axial-symmetric Euler equations, equations of state, finite volumes, Osher-type schemes, limiters, source terms, explicit time integration.

1 Introduction

1.1 Problem definition and paper outline

Hydraulic shock absorbers find their main application in vehicles (trains, cars, motor-cycles, ...). A major challenge in designing new hydraulic shock absorbers is to predict and prevent unwanted high-frequency phenomena in the interior oil flow. For that purpose, the availability of a state-of-the-art computational method for hydro- (i.e. oleo-) dynamics would be helpful. At the KONI company a start has been made in developing and applying such a method.

After a brief outline of construction and principles of a typical shock-absorber design (Section 1.2), in Section 2 its geometry and oleodynamics are modelled. In Section 3 the numerical method is presented: first the space discretization method for the system of equations that describe the oil flow (Section 3.1) and next the time-integration method (Section 3.2). The space discretization is partly new (a novel flux-difference splitting scheme for inviscid, compressible oil flow is presented). The time integration is standard (classical fourth-order accurate, four-stage Runge-Kutta). The paper ends with numerical results (Section 4) and concluding remarks (Section 5).

1.2 Brief outline of a shock-absorber design

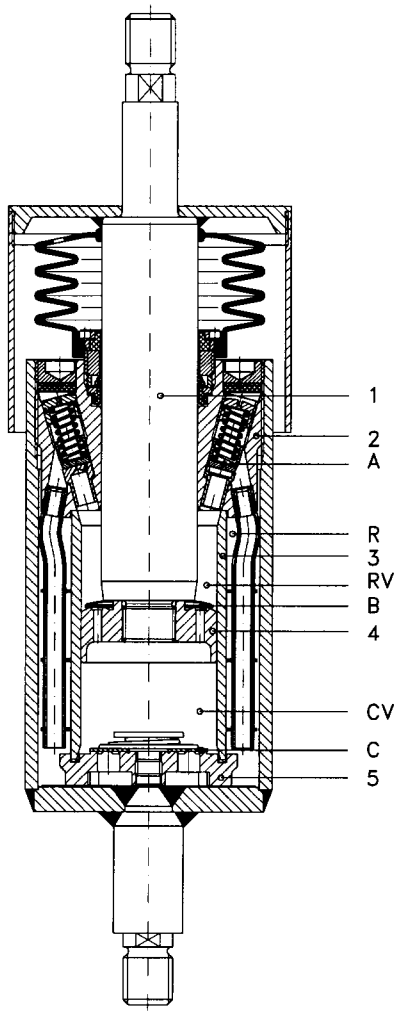

Figure 1: Cross-section of a shock-absorber design (© KONI): 1. piston rod, 2. guide, 3. inner cylinder, 4. piston, 5. foot assembly, A. damping valve, B. check valve, C. foot valve, CV. compression volume, RV. rebound volume, R. reservoir.

For the typical shock-absorber design depicted in Figure 1, a quick impression is given of the relevant construction parts and working principles. (For an extensive description, see [1].) The major parts of the shock absorber are a cylinder (3 in Figure 1) filled with oil (plus a small fraction of gas), and with a piston with rod in it (4 and 1 in Figure 1). The piston rod can move through a bearing, the guide (2 in Figure 1). With its lower pin the shock absorber can be mounted to e.g. a train bogie, in which case the piston rod can be mounted to e.g. the passenger cabin. (The mounting may also be the reverse; for the method described in this paper it is not essential what is mounted to what.) The piston will be set into motion by an external axial force experienced by the vehicle. To this force, a good shock absorber reacts with an (almost) equally large and (almost) equally synchronous counter-force exerted by the oil. During an inward piston stroke (compression stroke), the oil flows through orifices in the piston from the lower piston clearance (the compression volume, CV in Figure 1) into the upper piston clearance (the rebound volume, RV in Figure 1). The piston orifices are normally shut off by a valve (the check valve, B in Figure 1), which is held in its place by a spring. (The check valve inhibits the oil to flow into the reverse direction during an outward piston stroke.) To compensate for volume occupied by the piston

rod during a compression stroke, oil flows through orifices in the guide, into the spacing (the reservoir, R in Figure 1) in between the cylinder with piston and a secondary outer cylinder. The orifices in the guide are usually shut off as well (by the so-called damping valves, A in Figure 1). From the reservoir the oil can flow into the compression volume. During the compression stroke this will not occur, since then the pressure in the compression volume is higher than in the reservoir. But during the following outward piston stroke the pressure in the compression volume becomes lower than in the reservoir and oil will flow from the reservoir through the foot valve (C and 5 in Figure 1), back into the compression volume. The points and durations of time of the various valve movements play an important role in the proper working of the shock absorber. This holds in particular for the damping valves.

Concerning unwanted high-frequency oil-flow phenomena (reaction forces) that may be generated in a shock absorber, more or less generally accepted hypotheses are that these can be due to the waterhammer effect or to cavitation in the oil flow. But here we hypothesize that these spurious forces are mainly related to pressure waves travelling to and fro in the rebound volume. The waves are supposed to reflect at closed damping and check valves. During reflection of the waves, the damping valves may quickly open (and close), violating design principles. These spurious movements of the damping valves may cause high-frequency pressure perturbations that may be transmitted directly (through construction parts) to the passenger cabin. In the next section we propose a mathematical-physical model for oil flow in the rebound volume. The model allows a first investigation of the pressure-wave hypothesis.

2 Oil-flow modelling in rebound volume

2.1 Geometry

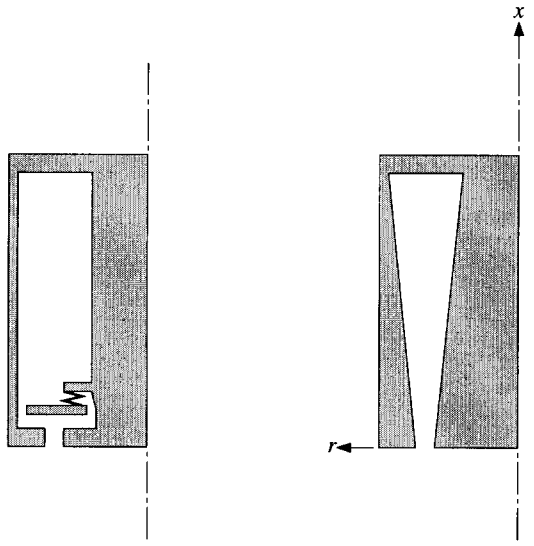

a. Axial-symmetric, with damping valve closed and check valve opened.

b. Without forward and backward facing steps.

Figure 2: Schematized rebound volumes.

The rebound volume, as depicted in Figure 1, is almost axially symmetric. For simplicity, we approximate it as axial-symmetric. Further we take the damping valve closed and the check valve opened. A sketch is given in Figure 2a. A difficulty of the geometry in Figure 2a in case of inviscid fluid-flow computations is that no unique solution exists for it; in its backward-facing-step regions, vortices of arbitrary strength are allowed. To ensure uniqueness in the case of inviscid oil-flow computations we remove all steps, see Figure 2b.

2.2 Oil-flow equations

To investigate the effects of propagating pressure waves, an inviscid model suffices. To include nonlinear effects (shocks) and to facilitate future extensions of the flow model, as governing equations we take the Euler equations, in axial-symmetric coordinates (Figure 2b) given by:

$$\frac{\partial q}{\partial t} + \frac{\partial f(q)}{\partial x} + \frac{\partial g(q)}{\partial r} = -\frac{1}{r} S(q), \tag{1a}$$

with q the state vector

$$q = \begin{pmatrix} \rho \\ \rho u \\ \rho v \end{pmatrix}, \tag{1b}$$

$f(q)$ and $g(q)$ the flux vectors

$$f(q) = \begin{pmatrix} \rho u \\ \rho u^2 + p \\ \rho uv \end{pmatrix}, \quad g(q) = \begin{pmatrix} \rho v \\ \rho vu \\ \rho v^2 + p \end{pmatrix}, \tag{1c}$$

and $S(q)$ the source vector

$$S(q) = \begin{pmatrix} \rho v \\ \rho vu \\ \rho v^2 \end{pmatrix}. \tag{1d}$$

Here u and v denote the velocity components in axial (x-) and radial (r-) direction, respectively, and ρ denotes the density and p the pressure.

The system is completed by the equation of state, discussed in the next section.

2.3 Equation of state and speed of sound for oil

2.3.1 Equation of state

We assume that the absorber is completely filled with oil. For oil, an equation of state is not readily available. According to [2], a suitable engineering model is

$$\begin{aligned} p - p_0 = &\left[A_1 \left(\frac{\rho}{\rho_0} - 1 \right) + A_2 \left(\frac{\rho}{\rho_0} - 1 \right)^2 + A_3 \left(\frac{\rho}{\rho_0} - 1 \right)^3 \right] \\ + &\left[B_0 + B_1 \left(\frac{\rho}{\rho_0} - 1 \right) + B_2 \left(\frac{\rho}{\rho_0} - 1 \right)^2 + B_3 \left(\frac{\rho}{\rho_0} - 1 \right)^3 \right] \rho_0 c_v \left(T - T_0 \right). \end{aligned} \tag{2}$$

In (2), c_v denotes the specific heat at constant density, T the temperature, and the subscript 0 (in p_0, ρ_0, T_0) refers to a specific reference state. For various types of oil, A_i, B_i and c_v are known. By incorporating the energy equation into (1), with (2) we would then have a closed set of equations. However, in our present pilot model we do not yet want to include temperature; it seems that temperature dependence can be neglected as a first approximation. Support for this comes from computing practice for compressible water flows. For water one uses as equation of state Tait's classical formula

$$\frac{\frac{p}{p_0} + B}{1 + B} = \left(\frac{\rho}{\rho_0} \right)^n, \tag{3}$$

see [3] for the original publication and e.g. also [4], p. 56 or [5], p. 102. In (3), p_0 and ρ_0 are again a reference pressure and density, and n and B are parameters. For water n and B are known, for oil both are unknown. In analogy with (3), we neglect temperature dependence in (2). To further simplify (2) we also neglect the nonlinear terms, yielding as the equation of state that we are going to use:

$$p - p_0 = A_1 \left(\frac{\rho}{\rho_0} - 1 \right). \tag{4}$$

So in fact (4) is a linearized version of Tait's equation (3).

2.3.2 Speed of sound

The equation of state (4) implies isentropy, because no other function $p = p(\rho)$ can exist of course, that describes isentropy for any arbitrary state. Hence, (4) may be substituted into the general definition of the speed of sound:

$$c = \sqrt{\left(\frac{\mathrm{d}p}{\mathrm{d}\rho}\right)_s}, \tag{5}$$

where the subscript s refers to isentropic conditions. Substitution yields

$$c = c_0 \equiv \sqrt{\frac{A_1}{\rho_0}}. \tag{6}$$

2.4 Boundary and initial conditions

System (1) is hyperbolic with respect to time. Therefore the number of conditions to be imposed at a boundary should equal the number of characteristics entering the domain at that boundary. Two types of boundaries occur in the rebound volume's geometry as depicted in Figure 2b:

- solid impermeable wall, and
- subsonic inflow.

Interpreting a solid impermeable wall as the limit of subsonic outflow, the number of boundary conditions to be imposed there should equal one. (As is standard, a zero normal velocity component will be imposed.) Across a subsonic inflow boundary, for the present system of three equations, two characteristics enter the domain, which implies that the number of boundary conditions to be imposed there should be two. In the present case, by these two subsonic inflow conditions the opening and closing of the check valve should be modelled. We refrain from introducing a complete model of the valve's dynamics. Only the check valve's kinematics is modelled and merely implicitly, viz. by specifying the velocity component normal to the boundary as a function of time: $u(x = 0, r, t) = u_{\mathrm{in}}(t)$, given in Figure 3. The valve's closing is simply taken as a discontinuity in time: at $t = t_1$, u_{in} drops instantaneously from $(u_{\mathrm{in}})_{\mathrm{max}}$ to zero. The values of $(u_{\mathrm{in}})_{\mathrm{max}}$ and t_1 can be varied by the user. As the second condition at the inflow boundary, we simply impose a zero tangential velocity component: $v(x = 0, r, t) = 0$, $t \geq 0$.

All boundary conditions imposed concern the oil's kinematics only; pressure (or density) is not imposed at any boundary. The pressure is put on a proper value through the initial conditions. As the initial solution we take the hydrostatic one: $u(x, r, t = 0) = v(x, r, t = 0) = 0$ and $p(x, r, t = 0) = p_0$, where p_0 can be chosen by the user.

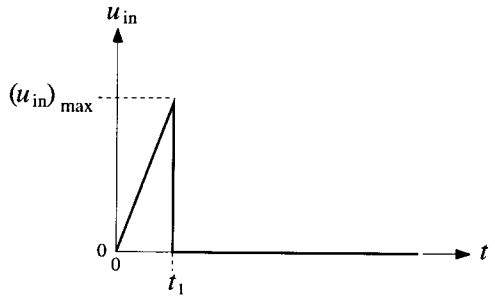

Figure 3: Sawtooth-type inflow velocity.

3 Numerical method

To allow for discontinuous solutions, following Lax [6], the system of equations (1a) is rewritten in the integral form

$$\iint_{\Omega^*} \frac{\partial q}{\partial t} \mathrm{d}x\mathrm{d}r + \oint_{\partial\Omega^*} (f(q)\cos\phi + g(q)\sin\phi)\,\mathrm{d}s = \iint_{\Omega^*} -\frac{1}{r}S(q)\mathrm{d}x\mathrm{d}r, \tag{7}$$

where Ω^* is an arbitrary subdomain of the computational domain Ω, $\partial\Omega^*$ the boundary of Ω^*, and $\cos\phi$ and $\sin\phi$ the x- and r-components of the outward unit normal on $\partial\Omega^*$. For the present low-subsonic oil-flow computations, use of the integral form is not as mandatory as in e.g. supersonic gasdynamics. However, no reasons exist for not applying it. In the discretization of (7) we follow the method-of-lines approach, so the spatial discretization and the temporal integration are considered separately.

3.1 Space discretization

A straightforward space discretization is obtained by subdividing Ω, in a structured manner, into disjunct non-overlapping subdomains $\Omega_{i,j}$, $i = 1,2,\ldots,M$, $j = 1,2,\ldots,N$ (finite volumes). As type of finite-volume discretization we take the cell-centred one. As finite-volume shapes, we will allow arbitrarily shaped quadrilaterals, the structured subdivision being such that $\Omega_{i+1,j}, \Omega_{i-1,j}, \Omega_{i,j+1}$ and $\Omega_{i,j-1}$ are the neighbouring volumes of $\Omega_{i,j}$ (Figure 4).

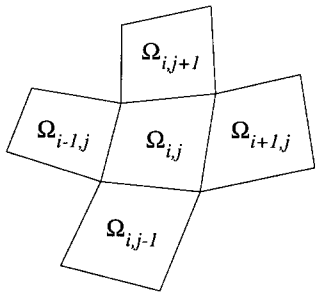

Figure 4: Quadrilateral finite volume and its neighbours.

Using the rotational invariance of the flux-vector part from the axial-symmetric Euler equations:

$$f(q)\cos\phi + g(q)\sin\phi = T^{-1}(\phi)f(T(\phi)q), \tag{8a}$$

with $T(\phi)$ the rotation matrix

$$T(\phi) = \begin{pmatrix} 1 & 0 & 0 \\ 0 & \cos\phi & \sin\phi \\ 0 & -\sin\phi & \cos\phi \end{pmatrix}, \tag{8b}$$

for finite volume $\Omega_{i,j}$ (7) can be rewritten as

$$\iint_{\Omega_{i,j}} \frac{\partial q}{\partial t} \mathrm{d}x\mathrm{d}r + \oint_{\partial\Omega_{i,j}} T^{-1}(\phi)f(T(\phi)q)\mathrm{d}s = \iint_{\Omega_{i,j}} -\frac{1}{r}S(q)\mathrm{d}x\mathrm{d}r. \tag{9}$$

Concerning the space discretization part of (9), it appears that per finite volume we need to evaluate

- the net flux of mass and momentum along $\partial\Omega_{i,j}$, and
- the source term integrated over $\Omega_{i,j}$.

3.1.1 Flux evaluation

For the present problem, a numerical flux function needs to be chosen which accurately models the propagation of pressure waves. In our opinion, for this purpose upwind schemes are better suited than central schemes. The most promising upwind schemes are the multi-dimensional ones (see e.g. [7, 8] for some genuinely multi-D upwind schemes, or [9, 10, 11, 12] for some simpler multi-D upwind schemes). The most well-proven upwind schemes are all 1-D. Examples of these are the schemes that follow the Godunov approach [13] (the flux-difference splitting schemes as Osher's [14] and Roe's [15]), or the schemes that are in fact based on a particle approach (the flux splitting schemes as Van Leer's [16] and Steger & Warming's [17]). Because it is not yet clear whether the multi-D upwind schemes will be more accurate for a given computational cost than the 1-D upwind schemes, here we stick to the latter. All aforementioned 1-D upwind schemes have in common that along each cell face the flux vector is assumed to be constant and to be determined by uniformly constant left and right cell-face states q_l and q_r only. Hence, for these schemes (9) can be rewritten as

$$\begin{aligned}\iint_{\Omega_{i,j}} \frac{\partial q}{\partial t}\mathrm{d}x\mathrm{d}r + T^{-1}(\phi_{i+\frac{1}{2},j})F\left(T(\phi_{i+\frac{1}{2},j})(q_l)_{i+\frac{1}{2},j}, T(\phi_{i+\frac{1}{2},j})(q_r)_{i+\frac{1}{2},j}\right) l_{i+\frac{1}{2},j} + \\ T^{-1}(\phi_{i,j+\frac{1}{2}})F\left(T(\phi_{i,j+\frac{1}{2}})(q_l)_{i,j+\frac{1}{2}}, T(\phi_{i,j+\frac{1}{2}})(q_r)_{i,j+\frac{1}{2}}\right) l_{i,j+\frac{1}{2}} + \\ T^{-1}(\phi_{i-\frac{1}{2},j})F\left(T(\phi_{i-\frac{1}{2},j})(q_l)_{i-\frac{1}{2},j}, T(\phi_{i-\frac{1}{2},j})(q_r)_{i-\frac{1}{2},j}\right) l_{i-\frac{1}{2},j} + \\ T^{-1}(\phi_{i,j-\frac{1}{2}})F\left(T(\phi_{i,j-\frac{1}{2}})(q_l)_{i,j-\frac{1}{2}}, T(\phi_{i,j-\frac{1}{2}})(q_r)_{i,j-\frac{1}{2}}\right) l_{i,j-\frac{1}{2}} = \\ \iint_{\Omega_{i,j}} -\frac{1}{r}S(q)\mathrm{d}x\mathrm{d}r, \end{aligned} \tag{10}$$

where $F\left(T(\phi_{i+\frac{1}{2},j})(q_l)_{i+\frac{1}{2},j}, T(\phi_{i+\frac{1}{2},j})(q_r)_{i+\frac{1}{2},j}\right)$ e.g., represents the transport of mass, momentum and energy (per unit of length and time) across $\partial\Omega_{i+\frac{1}{2},j}$, and where $l_{i+\frac{1}{2},j}$ denotes the length of $\partial\Omega_{i+\frac{1}{2},j}$ (Figure 5).

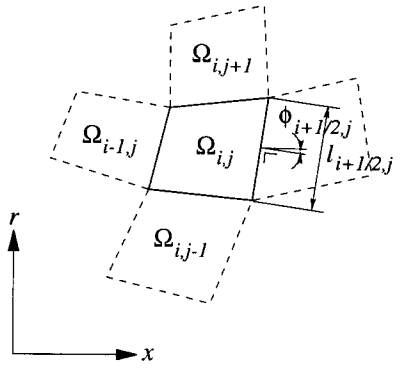

Figure 5: Quadrilateral finite volume and the geometric quantities needed for a single flux computation.

For this so-called numerical flux function $F(q_l, q_r)$, we prefer a scheme of flux-difference splitting type. As shown in [18, 19], flux-difference splitting schemes render better resolved shear layers (particularly contact discontinuities). Concerning the choice between an Osher- or Roe-type flux-difference splitting scheme, we prefer the Osher-type since it directly gives a physically proper boundary-condition treatment. Another advantage of an Osher-type scheme is its continuous differentiability, which allows the application of an implicit solution method employing flux derivatives.

For the present set of equations, (1) and (4), the corresponding Osher-type scheme does not yet exist. It will be constructed hereafter.

An Osher-type scheme for 2-D isentropic Eulerian oil flow In Osher-type schemes, the numerical flux function $F(q_l, q_r)$ is defined as

$$F(q_l, q_r) = f(q_l) + \int_{q_l}^{q_r} \frac{\mathrm{d}f(q)}{\mathrm{d}q}^{-} \mathrm{d}q =$$
$$f(q_r) - \int_{q_l}^{q_r} \frac{\mathrm{d}f(q)}{\mathrm{d}q}^{+} \mathrm{d}q =$$
$$\frac{1}{2}\left(f(q_l) + f(q_r)\right) - \frac{1}{2}\int_{q_l}^{q_r} \left| \frac{\mathrm{d}f(q)}{\mathrm{d}q} \right| \mathrm{d}q, \tag{11}$$

where $\frac{\mathrm{d}f(q)}{\mathrm{d}q}^{-}$ is the negative eigenvalue part of $\frac{\mathrm{d}f(q)}{\mathrm{d}q}$, $\frac{\mathrm{d}f(q)}{\mathrm{d}q}^{+}$ the positive eigenvalue part, and where $\left| \frac{\mathrm{d}f(q)}{\mathrm{d}q} \right| \equiv \frac{\mathrm{d}f(q)}{\mathrm{d}q}^{+} - \frac{\mathrm{d}f(q)}{\mathrm{d}q}^{-}$. Osher has proposed integration paths in state space (for the integrals in (11)) that make the integration trivial. For theoretical background and an impression how an Osher-type scheme is constructed, see [14]. (There the construction is done for the hyperbolic systems that describe 1-D non-isentropic Lagrangian gas flow, 1-D non-isentropic Eulerian gas flow, and 2-D isentropic Eulerian gas flow.) To construct an Osher-type scheme for the present 2-D Eulerian oil flow described by (1) and (4), only the homogeneous quasi-linear form

$$\frac{\partial q}{\partial t} + \frac{\mathrm{d}f(q)}{\mathrm{d}q}\frac{\partial q}{\partial x} = 0 \tag{12}$$

needs to be considered. With q according to (1b), $f(q)$ according to (1c), $p(\rho)$ according to (4), and the speed of sound c_0 according to (6), for the Jacobian $\frac{\mathrm{d}f(q)}{\mathrm{d}q}$ it follows then

$$\frac{\mathrm{d}f(q)}{\mathrm{d}q} = \begin{pmatrix} 0 & 1 & 0 \\ -u^2 + c_0^2 & 2u & 0 \\ -uv & v & u \end{pmatrix}. \tag{13}$$

The eigenvalues of the Jacobian are

$$\lambda_1 = u - c_0, \quad \lambda_2 = u, \quad \lambda_3 = u + c_0. \tag{14}$$

The fact that the eigenvalues vary with u only (since c_0 is constant) means that steepening of solution gradients (i.e. the nonlinearity) comes from u only. The eigenvectors corresponding with the above eigenvalues are

$$R_1 = \begin{pmatrix} \frac{1}{v} \\ \frac{u-c_0}{v} \\ 1 \end{pmatrix}, \quad R_2 = \begin{pmatrix} 0 \\ 0 \\ 1 \end{pmatrix}, \quad R_3 = \begin{pmatrix} \frac{1}{v} \\ \frac{u+c_0}{v} \\ 1 \end{pmatrix}. \tag{15}$$

The eigenvectors are linearly independent. Referring to the theory in [14], R_2 is linearly degenerate, and R_1 and R_3 are genuinely nonlinear. Hence, R_1 and R_3 should correspond with simple waves (compression or expansion waves), and R_2 with a contact discontinuity. We consider now the integration path in state space. Osher has proposed to take a path built up of subcurves, where each subcurve is tangential (in state space) to one of the eigenvectors. With the present three eigenvectors, according to Osher the integration path is as depicted in Figure 6a. In this path the ordering of eigenvectors, when going from q_l to q_r is R_3, R_2, R_1. The reverse (R_1, R_2, R_3 in going from q_l to q_r) is also possible (Figure 6b). The idea of reversion stems from Hemker & Spekreijse [20], who (for the 2-D non-isentropic perfect-gas Euler equations) named the ordering proposed by Osher the O(riginal)-variant and their own the P(hysical)-variant. The advantage of the P-variant over the O-variant is its better computational efficiency, particularly for subsonic flow computations. This can be explained as follows. With the integration path tangential to the eigenvectors, the integral evaluation boils down to ordinary flux evaluations at a few points along the integration path. Because two of the three eigenvalues are nonlinear, and one linearly degenerate, this number of points is five at a maximum. For the fully subsonic flows to be considered here, with the P-variant it is only one (!): $F(q_l, q_r) = f(q_{\frac{1}{3}})$. (With the O-variant this

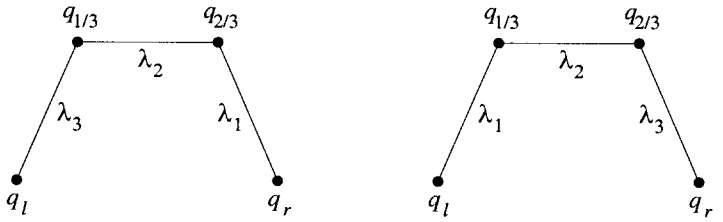

a. O-variant. b. P-variant.

Figure 6: Two variants of Osher-path in state space.

would be three: $F(q_l, q_r) = f(q_l) - f(q_{\frac{2}{3}}) + f(q_r)$.) Given the fact that the present computations are fully subsonic, here one can take full advantage of the P-variant.

To evaluate Osher's numerical flux function, the intersection states $q_{\frac{1}{3}}$ and $q_{\frac{2}{3}}$ need to be known. They follow from the Riemann invariants ψ_l^k, $k = 1,2,3$, $l = 1,2,3$, $l \neq k$ valid along the subcurves. The Riemann invariants satisfy

$$\nabla\psi_l^k \cdot R_k = 0, \quad k = 1,2,3, \quad l = 1,2,3, \quad l \neq k, \tag{16a}$$

$$\nabla \equiv \left(\frac{\partial}{\partial q_1}, \frac{\partial}{\partial q_2}, \frac{\partial}{\partial q_3}\right). \tag{16b}$$

Hence, ψ_l^2, $l = 1,3$ simply have to satisfy

$$\frac{\partial \psi_l^2}{\partial q_3} = 0, \quad l = 1,3. \tag{17}$$

These Riemann invariants follow directly, in conservative variables: $\psi_1^2 = q_1$, $\psi_3^2 = q_2$, or in primitive variables: $\psi_1^2 = \rho$, $\psi_3^2 = u$. (In case of a linearly degenerate eigenvalue one of the Riemann invariants is identical to that eigenvalue.) The Riemann invariants ψ_l^1, $l = 2,3$ along the first subcurve have to satisfy

$$q_1 \frac{\partial \psi_l^1}{\partial q_1} + (q_2 - c_0 q_1)\frac{\partial \psi_l^1}{\partial q_2} + q_3 \frac{\partial \psi_l^1}{\partial q_3} = 0, \quad l = 2,3. \tag{18}$$

The partial differential equation for the Riemann invariants along the third subcurve is almost identical to (18); it only differs in a sign in the second coefficient. (As a consequence, one of the corresponding Riemann invariants ψ_l^3, $l = 1,2$ will probably also have a difference with ψ_l^1, $l = 2,3$ in a single sign only.) Given the fact that both primitive variables ρ and u are constant along the second subcurve, they are no candidates for being a Riemann invariant along the first and third subcurve. The remaining primitive variable v *is*; substitution of $\psi_2^1 = \frac{q_3}{q_1}$ into (18) learns that it is a Riemann invariant indeed. So far, there is a good resemblance with the 2-D Eulerian gas case from [14]. Expecting a further resemblance, for the remaining Riemann invariant along the first subcurve we try $\psi_3^1 = u + Q(\rho) = \frac{q_2}{q_1} + Q(q_1)$. Substitution into (18) yields the simple ordinary differential equation $\frac{dQ}{dq_1} = \frac{c_0}{q_1}$. Integration yields $Q = c_0(\ln \rho + C)$, with C an integration constant. We take $C = -\ln \rho_0$, leading to the Riemann invariant $\psi_3^1 = u + c_0 \ln\left(\frac{\rho}{\rho_0}\right)$. It can be directly seen that along the third subcurve the Riemann invariants are: $\psi_1^3 = v$, $\psi_2^3 = u - c_0 \ln\left(\frac{\rho}{\rho_0}\right)$. The resulting Osher path is summarized in Figure 7. For the intersection states $q_{\frac{1}{3}}$ and $q_{\frac{2}{3}}$ it follows:

$$\begin{pmatrix} \rho_{\frac{1}{3}} \\ u_{\frac{1}{3}} \\ v_{\frac{1}{3}} \end{pmatrix} = \begin{pmatrix} \rho_{\frac{1}{2}} \\ u_{\frac{1}{2}} \\ v_l \end{pmatrix}, \quad \begin{pmatrix} \rho_{\frac{2}{3}} \\ u_{\frac{2}{3}} \\ v_{\frac{2}{3}} \end{pmatrix} = \begin{pmatrix} \rho_{\frac{1}{2}} \\ u_{\frac{1}{2}} \\ v_r \end{pmatrix}, \tag{19a}$$

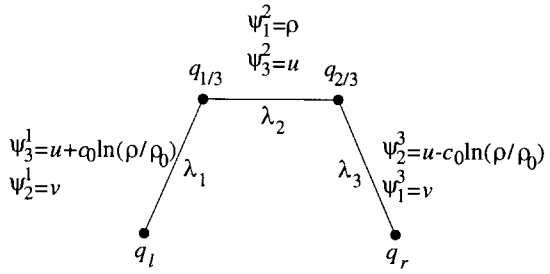

Figure 7: P-variant Osher-path for 2-D isentropic Eulerian oil flow.

where

$$\rho_{\frac{1}{2}} \equiv \sqrt{\rho_l \rho_r e^{\frac{u_l - u_r}{c_0}}}, \tag{19b}$$

$$u_{\frac{1}{2}} \equiv \frac{1}{2}(u_l + u_r) + \frac{1}{2} c_0 \ln\left(\frac{\rho_l}{\rho_r}\right). \tag{19c}$$

This concludes the construction of the present Osher scheme for given left and right cell-face states.

The Osher-type boundary-condition treatment for 2-D isentropic Eulerian oil flow If the cell face coincides with the boundary of the computational domain, in case of a left or right boundary, q_l or q_r, respectively, does not exist; it is outside the computational domain. Just *at* the boundary is the state q_b. This boundary state q_b can be determined by ingoing and outgoing characteristic information (i.e. by proper boundary conditions and Riemann invariants, respectively). An upwind treatment of boundary conditions fits well in Osher-type schemes. The theoretical basis for Osher's handling of boundary conditions is given in [21]. Following the same approach as in the foregoing section, here we will also mainly restrict ourselves to reinterpreting this theory in terms of the Osher-path. The reinterpretation will be done for the types of boundaries that we have to deal with here: subsonic inflow and solid impermeable wall.

Subsonic inflow In the present application we only have to deal with the case of a subsonic inflow boundary at the left (Figure 8a). For completeness, the case with boundary at the right (Figure 8b) is also considered.

a. Boundary at the left ($0 < u_r < c_r$). b. Boundary at the right ($-c_l < u_l < 0$).

Figure 8: The two cases of subsonic inflow boundary.

In both cases the Osher-path is reduced in the sense that one subcurve disappears (Figures 9a,b). The vanished subcurve corresponds with the outgoing characteristic. In both cases two of the three components of q_b should be given by boundary conditions. In Section 2.4 it has been decided to impose u_b and v_b. The remaining unknown component of q_b can be determined, together with the unknown state $q_{\frac{2}{3}}$ (left boundary) or $q_{\frac{1}{3}}$ (right boundary), by using the corresponding Riemann invariants ($\psi_1^2, \psi_3^2, \psi_1^3, \psi_2^3$

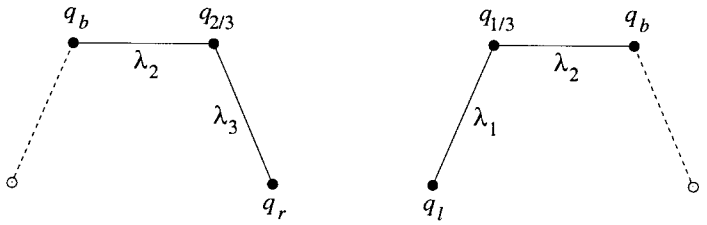

a. Boundary at the left ($0 < u_r < c_r$). b. Boundary at the right ($-c_l < u_l < 0$).

Figure 9: Reduced Osher-paths (P-variant) for subsonic inflow boundary.

for the left-boundary case and $\psi_2^1, \psi_3^1, \psi_1^2, \psi_3^2$ for the right). For the left-boundary case we find

$$\begin{pmatrix} \rho_b \\ u_b \\ v_b \end{pmatrix} = \begin{pmatrix} \rho_{\frac{1}{2}} \\ u_{\text{in}}(t) \\ 0 \end{pmatrix}, \quad \begin{pmatrix} \rho_{\frac{2}{3}} \\ u_{\frac{2}{3}} \\ v_{\frac{2}{3}} \end{pmatrix} = \begin{pmatrix} \rho_{\frac{1}{2}} \\ u_{\text{in}}(t) \\ v_r \end{pmatrix}, \tag{20a}$$

$$\rho_{\frac{1}{2}} = \rho_r \mathrm{e}^{\frac{u_{\text{in}}(t) - u_r}{c_0}}, \tag{20b}$$

and for the right (which is not in the present shock-absorber model):

$$\begin{pmatrix} \rho_{\frac{1}{3}} \\ u_{\frac{1}{3}} \\ v_{\frac{1}{3}} \end{pmatrix} = \begin{pmatrix} \rho_{\frac{1}{2}} \\ u_{\text{in}} \\ v_l \end{pmatrix}, \quad \begin{pmatrix} \rho_b \\ u_b \\ v_b \end{pmatrix} = \begin{pmatrix} \rho_{\frac{1}{2}} \\ u_{\text{in}} \\ v_{\text{in}} \end{pmatrix}, \tag{21a}$$

$$\rho_{\frac{1}{2}} = \rho_l \mathrm{e}^{\frac{u_l - u_{\text{in}}}{c_0}}. \tag{21b}$$

Solid impermeable wall In the present rebound-volume model both a left and a right wall (Figures 10a,b) occur.

a. Boundary at the left. b. Boundary at the right.

Figure 10: The two cases of solid impermeable wall boundary.

As mentioned in Section 2.4 only one component of q_b is prescribed by a boundary condition. The remaining two components are determined from the two Riemann invariants in the reduced Osher-path: ψ_1^3 and ψ_2^3 in the left-boundary case (Figure 11a), and ψ_2^1 and ψ_3^1 in the right-boundary case (Figure 11b). For the left-boundary case we find

$$\begin{pmatrix} \rho_b \\ u_b \\ v_b \end{pmatrix} = \begin{pmatrix} \rho_r \mathrm{e}^{\frac{-u_r}{c_0}} \\ 0 \\ v_r \end{pmatrix}, \tag{22}$$

and for the right-boundary case

$$\begin{pmatrix} \rho_b \\ u_b \\ v_b \end{pmatrix} = \begin{pmatrix} \rho_l e^{\frac{u_l}{c_0}} \\ 0 \\ v_l \end{pmatrix}. \tag{23}$$

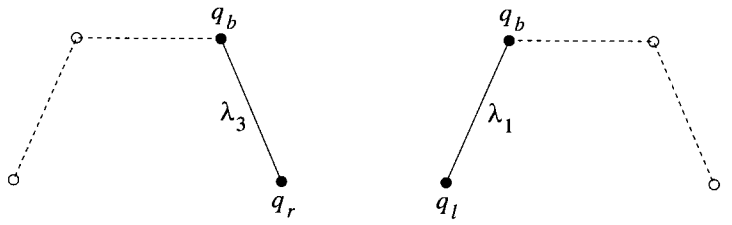

a. Boundary at the left. b. Boundary at the right.

Figure 11: Reduced Osher-paths (P-variant) for solid impermeable wall boundary.

This completes the boundary-condition treatment necessary for our application. Other types (subsonic outflow with pressure or outflow velocity specified, supersonic in- or outflow, ...) can be quickly constructed.

The interpolation for the left and right cell-face states To evaluate the four flux terms in (10), besides for the numerical flux function $F(q_l, q_r)$, a choice also needs to be made for its two arguments q_l and q_r. Both cell-face states are determined by interpolation through the neighbouring cell-centre states. The interpolation is done in a 1-D fashion, which is consistent with the application of a 1-D flux-difference splitting scheme. (Application of multi-D state interpolation in combination with a 1-D flux-difference splitting scheme is a possibility nevertheless [10, 22].) To discuss 1-D state interpolation in more detail, consider the 1-D set of cell faces given in Figure 12. (A similar set at constant i could also have been taken.)

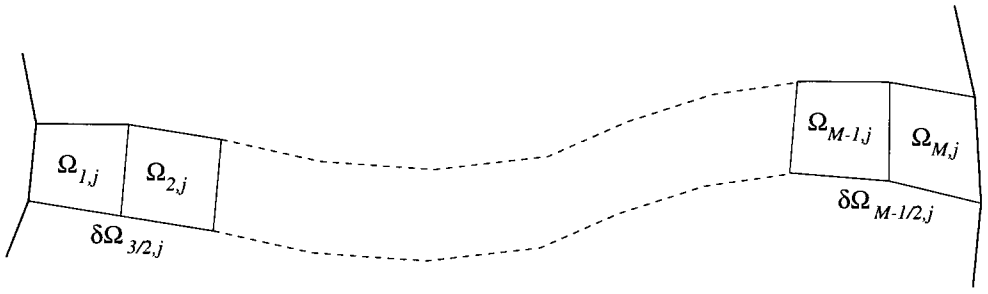

Figure 12: Line of cell-centred finite volumes (from boundary to boundary).

The simplest possible state interpolation is the first-order accurate one: $(q_l)_{i+\frac{1}{2},j} = q_{i,j}$, $(q_r)_{i-\frac{1}{2},j} = q_{i,j}$, $i = 1, 2, \ldots, M$. Its known advantages are its natural monotonicity and its applicability at all cell faces, $i = 1, 2, \ldots, M$. Its well-known disadvantages are its need for relatively fine grids in smooth flow regions and its strong smearing of discontinuities not aligned with the grid. We do not yet expect to get oblique discontinuities, but do appreciate a good accuracy-efficiency-ratio for smooth flows. Therefore the first-order accurate interpolation is not applied, but – instead – the higher-order accurate one:

$$(q_l)^k_{i+\frac{1}{2},j} = q^k_{i,j} + \frac{1}{2}\phi(r^k_{i+\frac{1}{2},j})(q^k_{i,j} - q^k_{i-1,j}), \quad r^k_{i+\frac{1}{2},j} = \frac{q^k_{i+1,j} - q^k_{i,j}}{q^k_{i,j} - q^k_{i-1,j}}, \quad i = 2, 3, \ldots, M-1, \quad k = 1, 2, 3, \tag{24a}$$

$$(q_r)^k_{i-\frac{1}{2},j} = q^k_{i,j} + \frac{1}{2}\phi(r^k_{i-\frac{1}{2},j})(q^k_{i,j} - q^k_{i+1,j}), \quad r^k_{i-\frac{1}{2},j} = \frac{q^k_{i-1,j} - q^k_{i,j}}{q^k_{i,j} - q^k_{i+1,j}}, \quad i = 2,3,\ldots,M-1, \quad k = 1,2,3, \tag{24b}$$

where the superscript k refers to the k-th solution component, and where $\phi(r)$ is the (monotonicity preserving) limiter function, for which the one from [23] is taken:

$$\phi(r) = \max(0, \min(2r, \min(\frac{1}{3} + \frac{2}{3}r, 2))). \tag{25}$$

This limiter is such that inside the monotonicity domain of Sweby [24] it coincides to the maximum extent with the for accuracy reasons favourable $\kappa = \frac{1}{3}$-scheme, see [25]. So far, limiter (25) has been applied to linear scalar advection problems only. The quality of the corresponding numerical results is satisfactory.

The interpolation formulas (24a) and (24b) cannot be applied up to and including the boundaries. There we apply the second-order upwind and the central interpolation formulas:

$$(q_r)_{\frac{1}{2},j} = q_{1,j} + \frac{1}{2}(q_{1,j} - q_{2,j}), \tag{26a}$$

$$(q_l)_{\frac{3}{2},j} = \frac{1}{2}(q_{1,j} + q_{2,j}), \tag{26b}$$

$$(q_r)_{M-\frac{1}{2},j} = \frac{1}{2}(q_{M-1,j} + q_{M,j}), \tag{26c}$$

$$(q_l)_{M+\frac{1}{2},j} = q_{M,j} + \frac{1}{2}(q_{M,j} - q_{M-1,j}). \tag{26d}$$

3.1.2 Source-term evaluation

The way of evaluating the source-term integral occurring in (7) is straightforward. $S(q)$ is taken piecewise constant over $\Omega_{i,j}$: $S(q) = S(q_{i,j})$ over $\Omega_{i,j}$. This directly leads to

$$\iint_{\Omega_{i,j}} -\frac{1}{r}S(q)\mathrm{d}x\mathrm{d}r = -\frac{1}{r_{i,j}}S(q_{i,j})A_{i,j}, \tag{27}$$

where $A_{i,j}$ is the area of finite volume $\Omega_{i,j}$. An alternative way of discretizing the source term is to first put it into the advection operator, and next to discretize this enhanced advection term with some arbitrary advection scheme. (As examples of such an advection-based discretization of source terms, see [23, 26, 27].) Given the fact that no spatial derivatives occur in (or can be easily introduced into) the present $S(q)$, this alternative source-term treatment is not feasible here.

3.2 Time integration

For the time discretization of the semi-discrete equation

$$\iint_{\Omega_{i,j}} \frac{\partial q}{\partial t}\mathrm{d}x\mathrm{d}r = R_{i,j}(\ldots, q_{i,j}, \ldots), \tag{28}$$

where $R_{i,j}(\ldots, q_{i,j}, \ldots)$ denotes the total space-discretization contribution in $\Omega_{i,j}$ (consisting of both the discrete flux and source-term contributions just discussed), we first rewrite (28) as

$$\frac{\partial q_{i,j}}{\partial t} = \frac{1}{A_{i,j}}R_{i,j}(\ldots, q_{i,j}, \ldots). \tag{29}$$

Equation (29) is integrated in time by the standard explicit four-stage Runge-Kutta scheme. Introducing the superscript n for the time level, then the computation of $q^{n+1}_{i,j}$ from $q^n_{i,j}$ can be written as:

$$q^1_{i,j} = q^n_{i,j} + \frac{1}{2}\tau\frac{1}{A_{i,j}}R_{i,j}((\ldots, q_{i,j}, \ldots)^n), \quad i = 1,2,\ldots,M, \quad j = 1,2,\ldots,N, \tag{30a}$$

$$q^2_{i,j} = q^n_{i,j} + \frac{1}{2}\tau\frac{1}{A_{i,j}}R_{i,j}((\ldots, q_{i,j}, \ldots)^1), \quad i = 1,2,\ldots,M, \quad j = 1,2,\ldots,N, \tag{30b}$$

$$q^3_{i,j} = q^n_{i,j} + \tau\frac{1}{A_{i,j}}R_{i,j}((\ldots, q_{i,j}, \ldots)^2), \quad i = 1,2,\ldots,M, \quad j = 1,2,\ldots,N, \tag{30c}$$

$$q^{n+1}_{i,j} = q^n_{i,j} + \frac{1}{6}\tau\frac{1}{A_{i,j}}\left[R_{i,j}((\ldots, q_{i,j}, \ldots)^n) + 2R_{i,j}((\ldots, q_{i,j}, \ldots)^1) + \right.$$
$$\left. 2R_{i,j}((\ldots, q_{i,j}, \ldots)^2) + R_{i,j}((\ldots, q_{i,j}, \ldots)^3)\right], \quad i = 1,2,\ldots,M, \quad j = 1,2,\ldots,N. \tag{30d}$$

The superscripts 1,2,3 refer to the intermediate stages of $q_{i,j}$, when integrating from t^n to t^{n+1}, and τ is the time step.

Formally, the time step is subjected to restrictions imposed by accuracy, stability and monotonicity. For a short overview of theory on monotonicity bounds for the time step, see [28]. (In fact in [28], instead of a monotonicity bound, a positivity bound is imposed on the time step, but in essence this is the same.) The stability bound imposed on the time step is the CFL-condition

$$\tau \leq \frac{h_{\min}\nu}{w_{\max}}. \tag{31}$$

In here $h_{\min}$ is the minimal grid size, $w_{\max}$ a maximum velocity (for which we take the preset value $(u_{\text{in}})_{\max}$), and ν the allowed CFL-number of explicit fourth-order accurate Runge-Kutta applied to the $\kappa = \frac{1}{3}$-discretized model equation $\frac{\partial c}{\partial t} + w_{\max}\frac{\partial c}{\partial x} = 0$. The accuracy bound on the time step is determined by the requirement that the sawtooth inlet velocity profile (Figure 3), particularly the jump at $t = t_1$, is imposed sufficiently accurate.

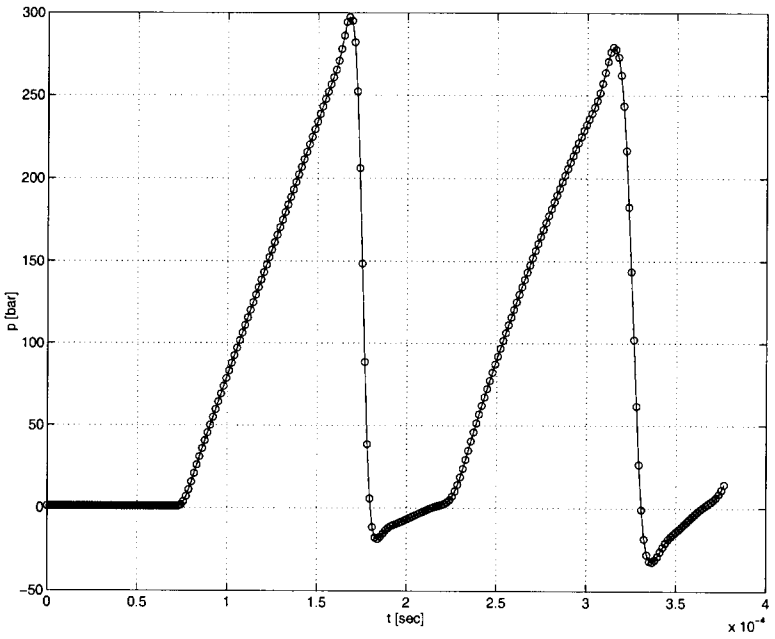

Figure 13: Beginning of pressure history in the middle of the rebound volume's upper boundary.

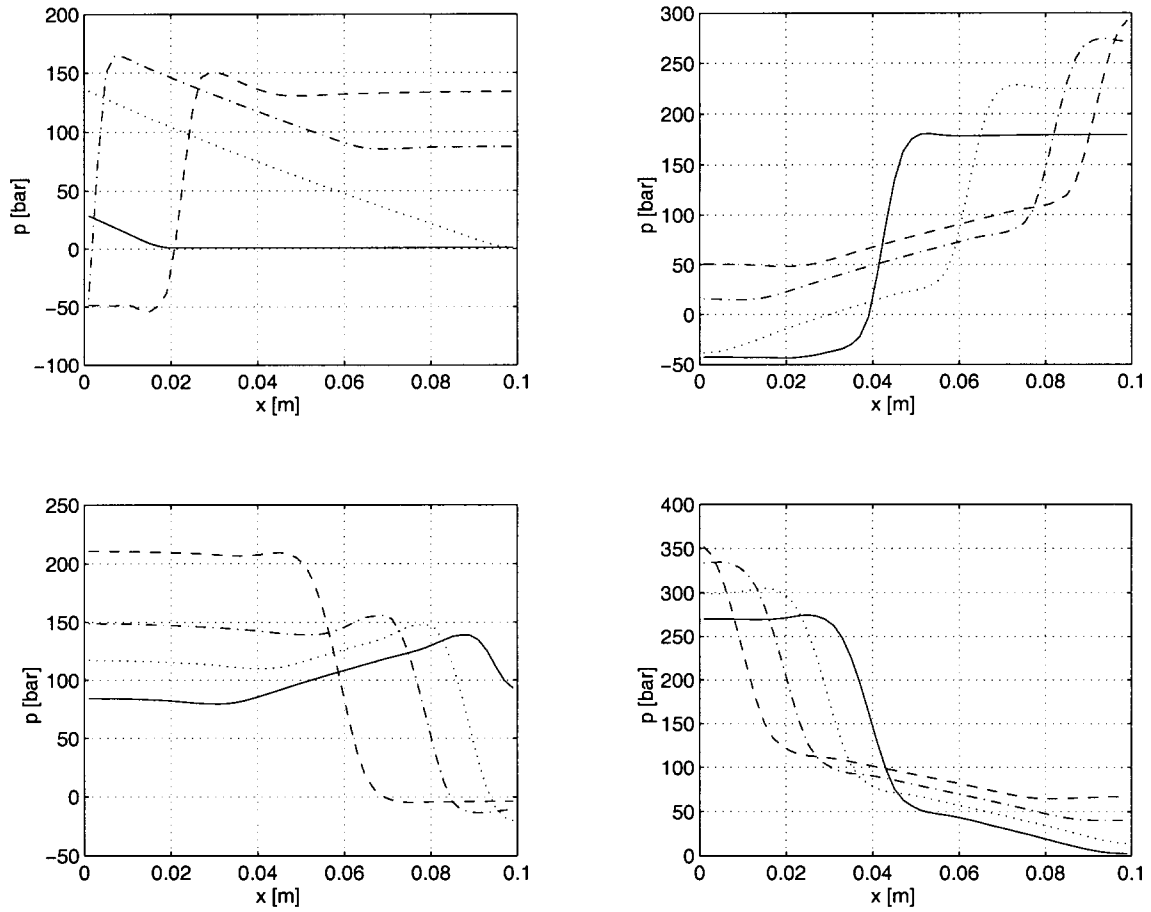

Figure 14: Beginning of pressure history along piston rod: 1. $t = 100\tau$, 2. $t = 500\tau$, 3. $t = 700\tau$, 4. $t = 800\tau$, 5. $t = 900\tau$, 6. $t = 1000\tau$, 7. $t = 1100\tau$, 8. $t = 1150\tau$, 9. $t = 1200\tau$, 10. $t = 1250\tau$, 11. $t = 1300\tau$, 12. $t = 1400\tau$, 13. $t = 1500\tau$, 14. $t = 1550\tau$, 15. $t = 1600\tau$, 16. $t = 1650\tau$, $\tau \approx 4.5 \times 10^{-7}$ sec.

4 Numerical results

For an elaborate presentation of numerical results, see [29]. Here a quick impression is given by presenting some representative results. The results have been obtained for the geometry given in Figure 2b, and for $p_0 = 1$ bar and $\rho_0 = 870$ kg/m^3.

In Figure 13 the beginning of a pressure history is depicted as computed in the middle of the rebound volume's upper boundary. The first pressure wave given in Figure 13 is directly caused by the check valve's opening. The second pressure wave is the reflection of the first wave. The graph shows the start of the travelling to and fro of pressure waves in the rebound volume. The negative pressures that are found are not believed to be a numerical artefact, but – instead – an illustration of the still existing shortcomings of the physical model, such as the zero diffusion and the lack of a cavitation model.

In Figure 14 pressure distributions are given along the piston rod at different times. The graphs show the evolution of a pressure wave during a single travel to and fro in the rebound volume. The pressure variations are large; unwanted opening of the damping valves may easily be the result.

To finish, in Figure 15 the possibility of studying the influence of parameters is shown, in Figure 15 that of A_1. As should be, the speeds of the pressure waves increase with increasing A_1.

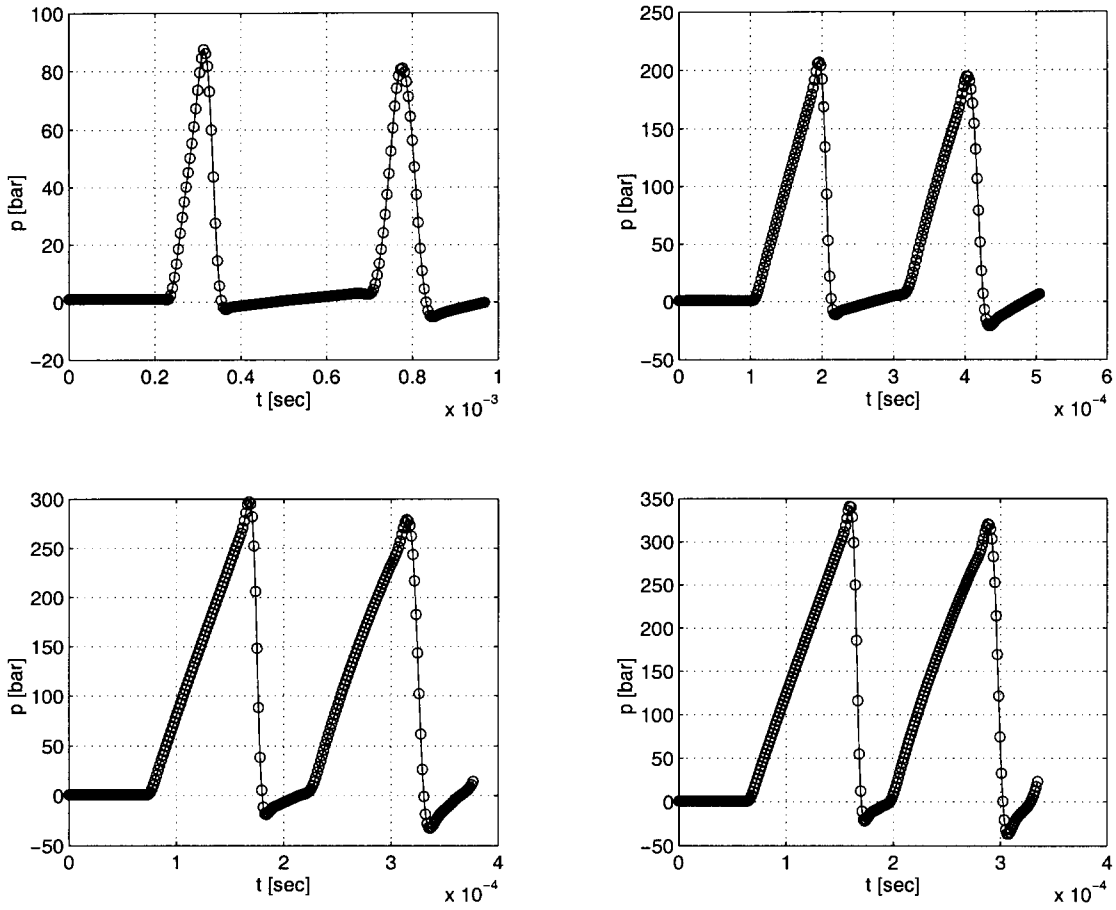

Figure 15: Beginning of pressure history in the middle of the rebound volume's upper boundary, for varying compressibility: a. $A_1 = 154$ bar, b. $A_1 = 1.6 \times 154$ bar, c. $A_1 = 10 \times 154$ bar, d. $A_1 = 13 \times 154$ bar.

5 Conclusions

From the viewpoint of shock-absorber design, many conclusions can be drawn, but here we restrict ourselves to the observation that the predicted pressure variations are large and may easily cause spurious opening and closing of valves.

Our first idea for future work is:

- to take the geometry closer to that given in Figure 1.

In case this extension introduces essentially multi-dimensional features (pressure waves propagating in various directions, not necessarily aligned with the grid), the application of a multi-D upwind discretization might be worthwhile. Our next ideas for future work concern the mathematical-physical model. We propose:

- to use an equation of state which takes into account multiphase behaviour,
- to introduce a cavitation model, and
- to extend the present Euler equations with viscous terms.

In case of the latter extension, the Osher scheme is certainly a good choice because of its good resolution of layers. Moreover, because of its continuously differentiable fluxes it is suitable for implicit time stepping, which may be necessary when viscous terms are added. Explicit time stepping remains an interesting possibility nevertheless. Recently, some new stability results were obtained for explicit time stepping applied to convection-diffusion equations [30].

Acknowledgment

The authors want to thank R. van Kasteel (KONI) and A. Segal (Delft University of Technology) for supporting this work.

References

[1] P.F.M. MICHIELSEN, RW-dempers, de werking van een RW-demper en de mogelijke geluidsoorzaken, Technical Report, KONI B.V., Oud-Beijerland (1994).

[2] P. BUIS AND A. VENIS, private communications, MacNeal-Schwendler, Gouda (1995).

[3] P.G. TAIT, *Voyage of H.M.S. Challenger*, **2**(4), H.M. Stationery Office, London (1889).

[4] G.K. BATCHELOR, *An Introduction to Fluid Dynamics*, Cambridge University Press, Cambridge (1983).

[5] P.A. THOMPSON, *Compressible-Fluid Dynamics*, McGraw-Hill, New York (1972).

[6] P.D. LAX, Hyperbolic systems of conservation laws II, *Communications on Pure and Applied Mathematics*, **10**, 537 (1957).

[7] CH. HIRSCH, C. LACOR AND H. DECONINCK, Convection algorithms based on a diagonalization procedure for the multidimensional Euler equations, *AIAA paper 87-1163* (1987).

[8] P.L. ROE, Discrete models for the numerical analysis of time-dependent multidimensional gas dynamics, *Journal of Computational Physics*, **63**, 458 (1986).

[9] S.F. DAVIS, A rotationally biased upwind difference scheme for the Euler equations, *Journal of Computational Physics*, **56**, 65 (1984).

[10] B. KOREN AND P.W. HEMKER, Multi-D upwinding and multigridding for steady Euler flow computations, in Proceedings of the Ninth GAMM Conference on Numerical Methods in Fluid Mechanics, Lausanne, 1991 (edited by (J.B. VOS, A. RIZZI AND I.L. RYHMING), *Notes on Numerical Fluid Mechanics*, **35**, pp. 89-98, Vieweg, Braunschweig (1992).

[11] D.W. LEVY, K.G. POWELL AND B. VAN LEER, An implementation of a grid-independent upwind scheme for the Euler equations, *AIAA paper 89-1931* (1989).

[12] C.L. RUMSEY, B. VAN LEER AND P.L. ROE, A grid-independent approximate Riemann solver with applications to the Euler and Navier-Stokes equations, *AIAA Paper 91-0239* (1991).

[13] S.K. GODUNOV, Finite difference method for numerical computation of discontinuous solutions of the equations of fluid dynamics (Cornell Aeronautical Laboratory Translation from the Russian), *Matematicheskii Sbornik* **47**, 271 (1959).

[14] S. OSHER AND F. SOLOMON, Upwind difference schemes for hyperbolic systems of conservation laws, *Mathematics of Computation*, **38**, 339 (1982).

[15] P.L. ROE, Approximate Riemann solvers, parameter vectors, and difference schemes, *Journal of Computational Physics*, **43**, 357 (1981).

[16] B. VAN LEER, Flux-vector splitting for the Euler equations, in Proceedings of the Eighth International Conference on Numerical Methods in Fluid Dynamics, Aachen, 1982 (edited by E. KRAUSE), *Lecture Notes in Physics*, **170**, pp. 507-512, Springer, Berlin (1982).

[17] J.L. STEGER AND R.F. WARMING, Flux vector splitting of the inviscid gasdynamic equations with application to finite-difference methods, *Journal of Computational Physics*, **40**, 263 (1981).

[18] B. VAN LEER, J.L. THOMAS, P.L. ROE AND R.W. NEWSOME, A comparison of numerical flux formulas for the Euler and Navier-Stokes equations, *AIAA paper 87-1104* (1987).

[19] B. KOREN, Upwind discretization of the steady Navier-Stokes equations, *International Journal for Numerical Methods in Fluids*, **11**, 99 (1990).

[20] P.W. HEMKER AND S.P. SPEKREIJSE, Multiple grid and Osher's scheme for the efficient solution of the steady Euler equations, *Applied Numerical Mathematics*, **2**, 475 (1986).

[21] S. OSHER AND S. CHAKRAVARTHY, Upwind schemes and boundary conditions with applications to Euler equations in general geometries, *Journal of Computational Physics*, **50**, 447 (1983).

[22] B. KOREN AND H.T.M. VAN DER MAAREL, Monotone higher-order accurate, multi-dimensional upwinding, in Proceedings of the 13th International Conference on Numerical Methods in Fluid Dynamics, Rome, 1992 (edited by M. NAPOLITANO AND F. SABETTA), *Lecture Notes in Physics*, **414**, pp. 110-114, Springer, Berlin (1993).

[23] B. KOREN, A robust upwind discretization method for advection, diffusion and source terms, in Numerical Methods for Advection-Diffusion Problems (edited by C.B. VREUGDENHIL AND B. KOREN), *Notes on Numerical Fluid Mechanics*, **45**, pp. 117-138, Vieweg, Braunschweig (1993).

[24] P.K. SWEBY, High resolution schemes using flux limiters for hyperbolic conservation laws, *SIAM Journal on Numerical Analysis*, **21**, 995 (1984).

[25] B. VAN LEER, Upwind-difference methods for aerodynamic problems governed by the Euler equations, in Proceedings of the 15th AMS-SIAM Summer Seminar on Applied Mathematics, Scripps Institution of Oceanography, 1983 (edited by B.E. ENGQUIST, S. OSHER AND R.C.J. SOMERVILLE), *Lectures in Applied Mathematics*, **22**(2), pp. 327-336, American Mathematical Society, Providence, RI (1985).

[26] P. GLAISTER, Flux difference splitting techniques for the Euler equations in non-Cartesian geometry, Numerical Analysis Report 8/85, Department of Mathematics, University of Reading (1985).

[27] P.L. ROE, Characteristic-based schemes for the Euler equations, *Annual Review of Fluid Mechanics*, **18**, 337 (1986).

[28] W. HUNDSDORFER, B. KOREN, M. VAN LOON AND J.G. VERWER, A positive finite-difference advection scheme, *Journal of Computational Physics*, **117**, 35 (1995).

[29] P.F.M. MICHIELSEN, Drukgolven als lawaai-oorzaak in schokdempers, M.Sc. Thesis, Faculty of Technical Mathematics and Informatics, Delft University of Technology (1995).

[30] P. WESSELING, Von Neumann stability conditions for the convection-diffusion equation, Report 95-48, Faculty of Technical Mathematics and Informatics, Delft University of Technology (1995).

Contents